Authors
Orang Alem, Rahul Mhaskar, Ricardo Jiménez-Martínez, Dong Sheng, John LeBlanc, Lutz Trahms, Tilmann Sander, John Kitching, and Svenja Knappe

Research Article | Vol. 25, No. 7 | 3 Apr 2017 | OPTICS EXPRESS 7849

Optics EXPRESS

Magnetic field imaging with microfabricated optically-pumped magnetometers

ORANG ALEM,[1,2,*] RAHUL MHASKAR,[1,2] RICARDO JIMÉNEZ-MARTÍNEZ,[1,2] DONG SHENG,[1,2] JOHN LEBLANC,[3] LUTZ TRAHMS,[4] TILMANN SANDER,[4] JOHN KITCHING,[1] AND SVENJA KNAPPE[1,2,]

[1]*National Institute of Standards and Technology, 325 Broadway, Boulder, CO 80305 USA*
[2]*University of Colorado, Boulder, CO 80309 USA*
[3]*C.S. Draper Laboratory, 555 Technology Sq., Cambridge, MA 02139 USA*
[4]*Physikalisch Technische Bundesanstalt, Abbestrasse 2-12, 10587 Berlin, Germany*
[*]*orangalem@gmail.edu*

Abstract: A multichannel imaging system is presented, consisting of 25 microfabricated optically-pumped magnetometers. The sensor probes have a footprint of less than 1 cm^2 and a sensitive volume of 1.5 mm × 1.5 mm × 1.5 mm and connect to a control unit through optical fibers of length 5 m. Operating at very low ambient magnetic fields, the sensor array has an average magnetic sensitivity of 24 $fT/Hz^{1/2}$, with a standard deviation of 5 $fT/Hz^{1/2}$ when the noise of each sensor is averaged between 10 and 50 Hz. Operating in Earth's magnetic field, the magnetometers have a field sensitivity around 5 $pT/Hz^{1/2}$. The vacuum-packaged sensor heads are optically heated and consume on average 76 ± 7 mW of power each. The heating power is provided by an array of eight diode lasers. Magnetic field imaging of small probe coils was obtained with the sensor array and fits to the expected field pattern agree well with the measured data.

OCIS codes: (120.4640) Optical instruments; (240.3990) Micro-optical devices; (280.3420) Laser sensors; (300.6210) Spectroscopy, atomic.

References and links

1. D. Le Sage, K. Arai, D. R. Glenn, S. J. DeVience, L. M. Pham, L. Rahn-Lee, M. D. Lukin, A. Yacoby, A. Komeili, and R. L. Walsworth, "Optical magnetic imaging of living cells," Nature **496**(7446), 486–489 (2013).
2. W. F. Stuart, "Earth's field magnetometry," Rep. Prog. Phys. **35**(2), 803–881 (1972).
3. E. Friis-Christensen, H. Lühr, and G. Hulot, "Swarm: A constellation to study the Earth's magnetic field," Earth Planets Space **58**(4), 351–358 (2006).
4. M. Acuña, "Fluxgate magnetometers for outer planets exploration," IEEE Trans. Magn. **10**(3), 519–523 (1974).
5. E. M. R. Forum, "Magnetic Resonance, a critical peer-reviewed introduction" (2014), retrieved http://www.magnetic-resonance.org/.
6. S. Supek and C. Aine, eds., *Magnetoencephalography - From Signals to Dynamic Cortical Networks* (Springer-Verlag Berlin Heidelberg, 2014), p. 1013.
7. J. B. Clarke, A. I., ed., *The SQUID Handbook* (Wiley-VCH, Weinheim, 2006), Vol. 2.
8. M. Pospelov, S. Pustelny, M. P. Ledbetter, D. F. J. Kimball, W. Gawlik, and D. Budker, "Detecting domain walls of axionlike models using terrestrial experiments," Phys. Rev. Lett. **110**(2), 021803 (2013).
9. O. Alem, T. H. Sander, R. Mhaskar, J. LeBlanc, H. Eswaran, U. Steinhoff, Y. Okada, J. Kitching, L. Trahms, and S. Knappe, "Fetal magnetocardiography measurements with an array of microfabricated optically pumped magnetometers," Phys. Med. Biol. **60**(12), 4797–4811 (2015).
10. Y. Ito, D. Sato, K. Kamada, and T. Kobayashi, "Measurements of Magnetic Field Distributions With an Optically Pumped K-Rb Hybrid Atomic Magnetometer," IEEE Trans. Magn. **50**, 1–3 (2014).
11. B. Patton, O. O. Versolato, D. C. Hovde, E. Corsini, J. M. Higbie, and D. Budker, "A remotely interrogated all-optical 87Rb magnetometer," Appl. Phys. Lett. **101**(8), 083502 (2012).
12. R. Mhaskar, S. Knappe, and J. Kitching, "A low-power, high-sensitivity micromachined optical magnetometer," Appl. Phys. Lett. **101**(24), 241105 (2012).
13. L. A. Liew, S. Knappe, J. Moreland, H. Robinson, L. Hollberg, and J. Kitching, "Microfabricated alkali atom vapor cells," Appl. Phys. Lett. **84**(14), 2694–2696 (2004).
14. M. J. Mescher, R. Lutwak, and M. Varghese, "An ultra-low-power physics package for a chip-scale atomic clock," The 13th International Conference on Solid-State Sensors, Actuators and Microsystems, 2005. Digest of Technical Papers. TRANSDUCERS '05., 2005, pp. 311–316 Vol. 1.
15. G. Wallis and D. Pomerantz, "Field Assisted Glass-Metal Sealing," J. Appl. Phys. **40**(10), 3946–3949 (1969).

#282368 https://doi.org/10.1364/OE.25.007849
Journal © 2017 Received 8 Dec 2016; revised 21 Jan 2017; accepted 23 Jan 2017; published 28 Mar 2017

Optics EXPRESS

16. J. Dupont-Roc, S. Haroche, and C. Cohen-Tannoudji, "Detection of very weak magnetic fields (10-9 gauss) by Rb zero-field level crossing resonances," Phys. Lett. A **28**(9), 638–639 (1969).
17. W. Happer and H. Tang, "Spin-Exchange Shift and Narrowing of Magnetic Resonance Lines in Optically Pumped Alkali Vapors," Phys. Rev. Lett. **31**(5), 273–276 (1973).
18. H. B. Dang, A. C. Maloof, and M. V. Romalis, "Ultrahigh sensitivity magnetic field and magnetization measurements with an atomic magnetometer," Appl. Phys. Lett. **97**(15), 151110 (2010).
19. V. Shah and M. V. Romalis, "Spin-exchange relaxation-free magnetometry using elliptically polarized light," Phys. Rev. A **80**(1), 013416 (2009).
20. C. Johnson, P. D. D. Schwindt, and M. Weisend, "Magnetoencephalography with a two-color pump-probe, fiber-coupled atomic magnetometer," Appl. Phys. Lett. **97**(24), 243703 (2010).
21. S.-K. Lee and M. V. Romalis, "Calculation of magnetic field noise from high-permeability magnetic shields and conducting objects with simple geometry," J. Appl. Phys. **103**(8), 084904 (2008).
22. M. Burghoff, T. H. Sander, A. Schnabel, D. Drung, L. Trahms, G. Curio, and B.-M. Mackert, "dc Magnetoencephalography: Direct measurement in a magnetically extremely-well shielded room," Appl. Phys. Lett. **85**(25), 6278–6280 (2004).
23. H. J. Lee, J. H. Shim, H. S. Moon, and K. Kim, "Flat-response spin-exchange relaxation free atomic magnetometer under negative feedback," Opt. Express **22**(17), 19887–19894 (2014).
24. S. J. Seltzer and M. V. Romalis, "Unshielded three-axis vector operation of a spin-exchange-relaxation-free atomic magnetometer," Appl. Phys. Lett. **85**(20), 4804–4806 (2004).
25. H. Dong, J. C. Fang, B. Q. Zhou, X. B. Tang, and J. Qin, "Three-dimensional atomic magnetometry," Eur. Phys. J. Appl. Phys. **57**(2), 21004 (2012).
26. W. E. Bell and A. L. Bloom, "Optically Driven Spin Precession," Phys. Rev. Lett. **6**(6), 280–281 (1961).
27. J. Preusser, V. Gerginov, S. Knappe, and J. Kitching, "A microfabricated photonic magnetometer," *2009 IEEE International Frequency Control Symposium Joint with the 22nd European Frequency and Time forum, Besancon, 2009, pp. 1180–1182.*
28. E. B. Alexandrov and A. K. Vershovskii, "Mx and Mz Magnetometers," in *Optical Magnetometry*, D. Budker and D. F. J. Kimball, eds. (Cambridge University Press, Cambridge, 2013), pp. 60–84.
29. "Eagle Technology," (Kanazawa, Japan).
30. M. Fuchs, H. A. Wischmann, M. Wagner, and J. Krüger, "Coordinate system matching for neuromagnetic and morphological reconstruction overlay," IEEE Trans. Biomed. Eng. **42**(4), 416–420 (1995).
31. R. Oostenveld, P. Fries, E. Maris, and J.-M. Schoffelen, "FieldTrip: Open source software for advanced analysis of MEG, EEG, and invasive electrophysiological data," Comput. Intell. Neurosci. **2011**, 156869 (2011).
32. G. Bison, N. Castagna, A. Hofer, P. Knowles, J. L. Schenker, M. Kasprzak, H. Saudan, and A. Weis, "A room temperature 19-channel magnetic field mapping device for cardiac signals," Appl. Phys. Lett. **95**(17), 173701 (2009).
33. H. Xia, A. B.-A. Baranga, D. Hoffman, and M. V. Romalis, "Magnetoencephalography with an atomic magnetometer," Appl. Phys. Lett. **89**(21), 211104 (2006).

1. Introduction

Magnetic imaging is a powerful tool that can be applied at many different spatial and temporal scales. On a very small scale, nitrogen vacancy color centers in diamond have been used to create magnetic images of living magnetotactic bacteria with sub-micrometer spatial resolution [1]. On a larger scale, magnetometers are routinely used to map areas of many square kilometers for prospecting, archeology, and magnetic anomaly detection [2]. On a very large scale, space-based magnetometers are used to map the magnetic field of the Earth [3] and other planets and their moons from satellites and spacecraft [4]. In medicine, magnetic resonance imaging (MRI) is a routine method to generate pictures of proton concentration in the human body with millimeter spatial resolution [5] and the technique of magnetoencephalography (MEG) maps the tiny currents in the brain with millisecond temporal resolution [6]. Other applications for magnetic imaging include nondestructive testing, surveillance, and microscopy [7]. There is even a suggestion to detect the magnetic field at many positions around the Earth with a time-synchronized network of magnetometers to aid in the search for dark matter and dark energy in the universe [8].

The magnetometers used for these imaging applications often trade off sensitivity for physical size. The fundamental sensitivity limit for most magnetic sensors is equivalent to an energy resolution $\delta B^2 V/2\mu_0$ on the order of the Planck's constant, where δB is the magnetic sensitivity, V is the volume, and μ_0 is the vacuum permeability. This results in a sensitivity of approximately 1 fT/√Hz for a volume of 1 mm^3, scaling as 1/√V. Other performance parameters such as bandwidth, linearity, slew rate, and dynamic range, as well as operational

Optics EXPRESS

parameters like size, power consumption, and possible array spacing also play a role in the choice of sensor for a particular application.

Here, we demonstrate an imaging array of 25 highly sensitive, microfabricated optically-pumped magnetometers (μOPM) that operate without cooling. The sensor heads are coupled to a common control unit through optical fibers of length 5 m, which determines the maximum spacing between sensors. The use of optical fibers allows for placement of the sensors in an arbitrary geometry around a source. Due to the small size of the sensor heads, they can be positioned very close to the area of interest, which can result in large signal strengths. The same sensor heads were used for magnetocardiography in a related publication [9]. Previously, a multichannel image of a coil has been evaluated with a very large OPM consisting of a single cell of volume $(5\ \text{cm})^3$, which restricted the relative position of the array channels to within that volume [10]. If a much larger array spacing than the fiber-coupled system is desired, our technology could also be implemented using a free-space laser beam to link the sensor head with the control unit [11]. This approach could also allow for inexpensive, microfabricated, and completely passive sensor heads that can remain dormant without consuming any power until optically heated and interrogated by light.

2. Design of the imaging array

A schematic of the imaging system is shown in Fig. 1. Optical fibers connect the sensor heads to a control unit that houses the lasers, the fiber splitter network, and the electronics. Two distributed-feedback lasers (DFB) at a wavelength of 795 nm provide sufficient light to interrogate the atoms while eight diode lasers at 1.5 μm heat the vapor cells in all the sensor heads. To reach the desired atomic vapor density, the cells are heated to roughly 150 °C using absorptive filters attached to the windows of the cells similar to the method described previously [12]. Optical fiber splitters distribute the heating and probing lights from the lasers to the 25 sensors. The control unit includes 25 transimpedance amplifiers to amplify the signals from the photodiodes within the sensor heads and a 24-bit DAC system to record the data.

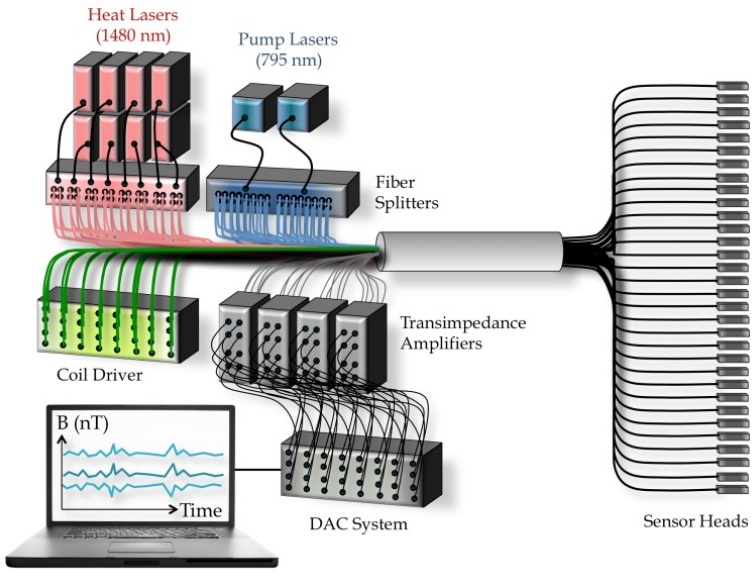

Fig. 1. Schematic of the magnetic imaging system.

Each sensor head contains a microfabricated vapor cell [13] with an internal volume of 1.5 mm × 1.5 mm × 1.5 mm, filled with ^{87}Rb and roughly 1 amagat of N_2. The size of the cell defines the sensitive volume of the magnetometers. The cells are suspended between two web

Optics EXPRESS

like sheets of 5 μm thick polyimide under tension (see Fig. 3a) to minimize the thermal conductivity between cell and ambient environment to less than 3 mW [14]. The suspensions were made by first spinning a 5 μm thick layer of a photo-definable polyimide onto a 300 μm thick Si wafer. After a thermal cure, the polyimide suspension geometries are defined photolithographically. A deep reactive ion etch (DRIE) process is used to remove most of the silicon, leaving a perimeter ring to hold the polyimide suspension. The perimeter ring geometry is replicated in silicon to fabricate a spacer ring. The vapor cells with the integrated glass filters are slightly taller than the combined top and bottom suspension and spacer rings so that when epoxied together, the vapor cell stack pushes the polyimide tethers into tension. The tensioned tethers provide mechanical support as well as thermal isolation. One additional thinner spacer ring is attached to the bottom suspension to ensure that the cell assembly will not touch any of the walls of the vacuum package. Epotek 353ND epoxy is used for the entire assembly due to its very low outgassing properties for vacuum compatibility and high temperature tolerance.

The vacuum package consists of a cavity etched in 3 mm thick silicon wafer with BOROFLOAT[1] glass window anodically bonded on one side [15]. After the thermal suspension unit is placed into a silicon enclosure, the entire assembly is evacuated and the top window anodically bonded to form the sealed unit. Vacuum packaging reduces the conductive losses through the air, which is estimated to increase the power requirement for achieving the same temperature to more than 200 mW. Radiative losses are estimated to be roughly 50 mW and are the primary heat loss mechanism of the vacuum package system. We fabricated 33 sensor heads and measured the total required power for optimal performance (Fig. 2). The values ranged between 60 and 140 mW, giving a mean heating power of 80 mW and a standard deviation of 13 mW.

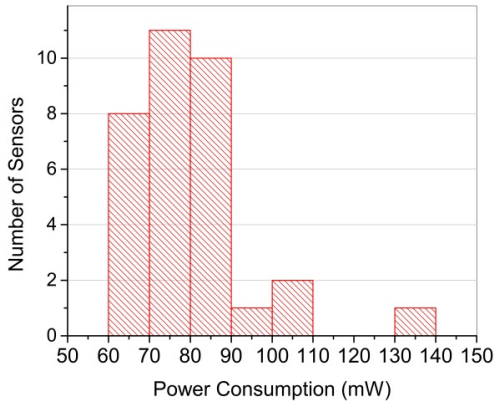

Fig. 2. Histogram of the power consumption of 33 sensors. The mean heating power is 80 mW with a standard deviation of 13 mW. Sensors with heating power above 90 mW were excluded from the final array, resulting in a mean power consumption of 76 ± 7 mW for the system.

We suspect that the differences in power consumption between the sensors is the results of different residual background gas pressures inside the packages. Powers have been measured repeatedly over the duration of 24 months and no significant changes in the required heating power have been observed. Sensors requiring above 90 mW of power were excluded from the array, resulting in a mean power consumption of 76 ± 7 mW. The vacuum packages have dimensions of 7.3 mm × 7.3 mm × 3.7 mm and a photograph is shown in Fig. 3a. A standoff distance of 3.65 mm between the center of the cell and the outside of the package defines the closest possible distance between the sensor and a magnetic source.

Optics EXPRESS

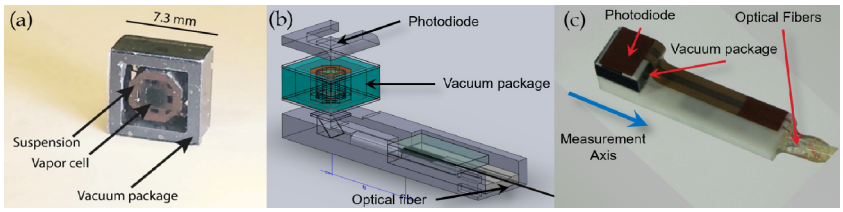

Fig. 3. (a) Photograph of a vacuum package. (b) Schematic of the sensor head. The optical fibers can be seen on the right side and the photodiode on top. (c) Photograph of a sensor head. The blue arrow indicates the direction of the modulation field and the detection axis of the magnetometer.

The two fibers for each sensor, a single-mode fiber transmitting the heating light and a polarization-maintaining fiber carrying the interrogation light, are terminated in a common ferrule made from V-grooves in silicon with 125 μm spacing. The ferrule, along with a microprism and a quarter waveplate are housed inside a Macor[1] optical bench. Both light beams exiting the optical fibers begin to diverge and are carefully spaced so that they expand to the desired size at the cell. Before reaching the cell, the beams are reflected at right angle by the microprism and then circularly polarized with the quarter-wave plate. While the heating light is absorbed by the colored glass filters, the interrogating light is unaffected, and is transmitted and detected by a photodiode mounted on a flexible polyimide circuit placed after the cell. A photograph of a sensor head is shown in Fig. 3c.

3. Performance

The magnetometer array can be operated in two modes, a zero-field mode and a total-field mode, as described below. In most of our experiments the magnetometers in the array were operated in a zero-field mode. This mode is based on the zero-field level-crossing resonance, first reported on by DuPont-Roc et al. [16], where the transmission of the circularly-polarized laser beam reaches a maximum at exactly zero transverse magnetic field. In this case, the macroscopic spin orientation does not precess around the magnetic field. Instead, a static repolarization results from the balance between optical pumping and precession of the atomic spins.

At high alkali densities, the zero-field mode benefits from high signal strength and a long coherence time. When the spin-exchange collision rate is much faster than the Larmor precession frequency, the dephasing of the spins due to spin-exchange collisions is suppressed [17]. This increases the sensitivity of the magnetometer in this mode of operation but limits the dynamic range to less than 100 nT. The bandwidth is typically a few hundred hertz, which is less than the total-field mode since the resonance line is narrower due to the suppression of spin-exchange broadening. A very high sensitivity has been measured by detecting the polarization rotation of a linearly-polarized probe light beam at right angle to the pump light [18]. Nevertheless, this polarimetry scheme is much more complicated to implement in small sensor heads. Several other schemes based on polarization rotation have also been proposed [19,20], where the pump and probe light beams are collinear.

To create a dispersive resonance lineshape, a modulated transverse magnetic field with an amplitude of approximately 50 nT and frequency of 1.6 kHz is applied using a set of Helmholtz coils imprinted on a flexible polyimide membrane that surrounds the sensor head. The photodiode signal is demodulated at the modulation frequency, generating the desired zero crossing of the signal at zero magnetic field. This phase-sensitive detection method shifts the signal from DC to the modulation frequency, thus avoiding the 1/f noise in the electronics. However, it also limits the maximum bandwidth to roughly one third of this frequency. The demodulator bandwidth was set to about 250 Hz, which was roughly equal to the intrinsic bandwidth of the atomic response.

Optics EXPRESS

Every sensor was separately evaluated inside a four-layer mu-metal shield with an additional inner ferrite layer in the shape of an octagonal prism of diameter 30 cm. The ferrite layer provides additional suppression of ambient magnetic field noise to a calculated value of 2 fT/Hz$^{1/2}$ at 1 Hz [21], providing a sufficiently low noise environment to characterize sensor performance. The sensitivity of each sensor was optimized in terms of cell temperature and laser power and the resonance slope and noise spectral density were recorded. Figure 4 shows the spectrum of the noise equivalent magnetic field from a subset of 16 arbitrarily chosen sensors (for clarity). Apart from a few spikes at 60 Hz and 120 Hz, the spectra appear to be mostly white up to the 3 dB bandwidth of 250 Hz. Below 10 Hz, the sensors suffer from 1/f noise, which require further tests to fully understand its origin. The histogram in the inset of Fig. 4 shows the noise distribution for 31 sensors averaged between 10 Hz and 50 Hz. In one sensor, the vacuum bond failed before the sensitivity could be evaluated. Of the 31 sensors, 26 sensors have sensitivities between 15 fT/Hz$^{1/2}$ and 30 fT/Hz$^{1/2}$ and only one sensor has a sensitivity above 40 fT/Hz$^{1/2}$.

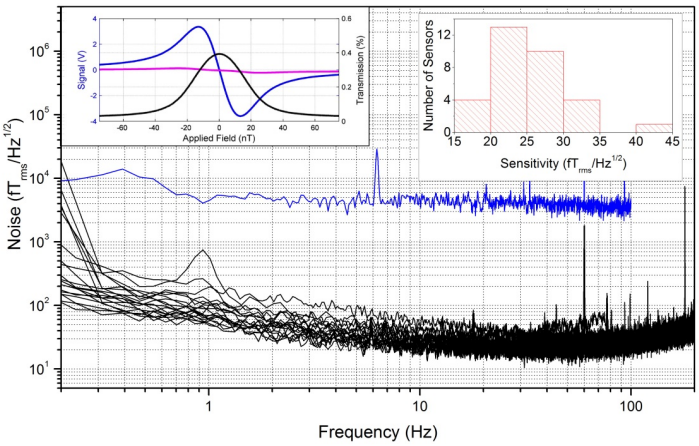

Fig. 4. Noise equivalent magnetic field of 16 sensors (from Ref [9].) as a function of frequency in the zero-field mode (black) and of one sensor in the total-field mode (blue). The left inset shows the light transmission (black), dispersive Lock-In signal (blue), and quadrature Lock-in output (magenta) as a function of magnetic field. The right inset shows the statistics of the 31 sensor sensitivities when averaged between 10 Hz and 50 Hz.

Following the individual sensor characterizations, an array of 25 sensors were assembled and operated simultaneously in the seven-layer magnetically-shielded room 'BMSR2' [22], which provided the optimal near zero-field conditions without the need for residual field compensation. Each of the eight heat lasers delivered power for up to four sensors while the two DFB lasers supplied the interrogation light to all the sensor in the array using the fiber splitter network. Two integrated optical fiber attenuators were used for every sensor to provide fine control of the pump and heating light intensities to ensure that all sensors were operated at their optimum sensitivity. The modulation field for phase-sensitive detection was set at the same frequency of 1.6 kHz for all the sensors and the phases chosen such that the modulation fields in neighboring sensors where phase-shifted by 180 degrees. We operated these sensors in an open-loop configuration where the demodulated photocurrent was used to measure the magnetic field once the slope of the dispersive resonance lineshape was calibrated at its zero-crossing point prior to every measurement.

The close proximity of the sensors in this configuration introduces the possibility of cross-talk from other nearby sensors. This cross-talk is manifest through a change in the modulation field amplitude and potentially the tilting of the field axis, which would alter the direction of the measured field components relative to the sensor axis. Based on of the distances between nearby sensors and the range of magnitudes and directions of the nearby modulation fields,

Optics EXPRESS

calculations indicate that this effect could in the worst case alter the measurement axis of a sensor by a tenth of a degree. To quantify the long-term gain stability in this configuration, determined by the slope of the magnetic resonance, we applied a 1 nT amplitude square wave magnetic field at a frequency of 1 Hz to the sensors using a coil. The output of one of the magnetometers was measured for one hour and the amplitude of the magnetic field step as measured by the magnetometer slowly decreased by 2.5% over a duration of this time. We verified that this was consistent with a decrease of the resonance slope. We suspect that one possibility is a slow drift of the pump laser polarization causing this change. A solution to improve the long-term gain stability from polarization fluctuations is to place a linear polarizer at the output of the fiber to maintain the polarization angle of the incident light and then lock the polarization induced intensity fluctuation by adding a monitor photodiode for each sensor and feeding back onto a variable optical fiber attenuator. A second cause for the drift of the magnetometer response may be due to a slow change in the ambient magnetic field on the order of the resonance linewidth. This would broaden or shift the magnetic resonance away from the zero-field resonance, where the output gain is optimal. Ensuring that the ambient field is within the linewidth of the magnetic resonance will maintain the response of the magnetometer within the linear regime of the resonance slop. To compensate, the magnetometers could be operated in a field-locked mode, where the change in the ambient field is compensated by applied fields using a set of three perpendicular coils around the sensor [23]. Similar methods have been demonstrated for Earth-field operation with zero-field magnetometers containing two perpendicular pump and probe beams [24] and was also proposed for the single-beam configuration used here [25]. While this method has the potential for good long-term stability, it is not easy to implement in a dense sensor array as the compensation field coils could easily cause interference between the sensors.

Thus far we have focused on the zero-field mode. Our imaging array can also operate in the total-field mode, which is best suited for applications at Earth's field [11]. We have previously demonstrated that sensors built in similar fashion can operate in the total-field mode by optically driving spin precession on resonance, i.e., so-called Bell-Bloom magnetometer [26]. In that work, we demonstrated sensitivities below 3 $pT/Hz^{1/2}$ and bandwidths of 1 kHz [27]. Another total-field magnetometer is the Mz configuration [28], that has the advantage of not requiring high-speed electronics and presents fewer heading errors. We have operated several sensors from this imaging array in Mz mode, where a modulation field is applied perpendicular to the pumping light at the Larmor frequency. A noise measurement from one sensor is shown in the main plot of Fig. 4 in blue, which represents similar sensitivities obtained across the sensors in the array operating in Mz mode.

4. Magnetic source localization with multichannel array

We arranged 21 sensors having the best performance to form an imaging array on a spherical plastic holder of diameter 20 cm such that the optical fibers point outward in the radial direction as is visible in Fig. 5a. The precise position of each sensor was determined from the known geometry of the openings in the plastic holder. A ratchet mechanism allowed for radial movement and registration of the sensor position in 5 mm increments. By noting the ratchet position and determining the sensor direction from the holder location, each sensor position was known with an error of less than 5 mm.

Five commercial probe coils of diameter 1 cm [29] were attached to a fiberglass sphere of diameter 19 cm, as shown in Fig. 5b. Two coils, labeled C1 and C2, in the field of view of the sensors, i.e., beneath the surface covered by the sensor array, were used to generate probe magnetic fields in the nT range, which is a signal strength orders of magnitude above the sensitivity limit. It was not the intention to generate test signals resembling neuronal fields. The coils are conductive trace windings etched into a double-layer printed circuit board and were supplied by a vendor. The precise coil geometry and the uncertainty in magnetic moment was not specified. A sketch of the geometry of the sensors in relation to the two

Optics EXPRESS

probe coils is shown in Fig. 5c to illustrate the experimental setup. The position of the fiberglass sphere in relation to the sensor array was manually adjusted with respect to the coil positions and could not be determined with high precision. The coils were sequentially energized 30 times for 400 ms durations by an applied oscillating current of 100 μA and frequency of 82 Hz. The resulting magnetic field distribution was measured continuously with our imaging array in the zero-field mode. After averaging the magnetic signal over the 30 sequential energizing cycles, the average is further reduced to a single field map for each coil through calculating the covariance between the known sinusoidal current generator signal and the signal recorded by each sensor. This procedure determines the amplitude and sign of the magnetic field from the coils as recorded by the sensors. A section of the averaged signal for coil 1 is shown in Fig. 6 which clearly shows that this coil is close to a group of four sensors on the left side of the array. Signal amplitudes are in the nanotesla range and well below saturation of the sensors. The field map obtained after the covariance calculation is shown in Fig. 7 (top left) and the peak in the map corresponds to the channels with maximum signal amplitude in Fig. 6. Instead of the combination of averaging and covariance calculation, a Fourier analysis can be applied for this type of marker coils, as is customary in SQUID magnetoencephalography systems [30].

Next, magnetic field of a dipole source at location $\vec{r}$ and magnetic moment $\vec{m}$, given by $\vec{B} = \frac{\mu_0}{4\pi r^3}\left(\frac{3(\vec{m}\cdot\vec{r})\vec{r}}{r^3} - \vec{m}\right)$ (e.g., [30]) was fitted to each of the coil maps. This forward model with six parameters (x,y,z position and x,y,z moment) is sufficiently stable for the 21 data points in each map. The result is shown in Fig. 7 with the field maps derived from the measured data on left, and the field maps resulting from the fit on the right. The small dots (hollow circles) in the colored region indicate the positions of the sensors in this two-dimensional representation of the actual three-dimensional geometry. These positions are the same as rendered in Fig. 5c. As mentioned before, coil C1 is located below and between four sensors, resulting in similar measured field amplitudes from those sensors; whereas coil C2 is located directly beneath one sensor with fewer sensors in its vicinity, and so the measured field from this sensor was much larger than the neighboring sensors. A fit with ordinary least squares was performed using the FieldTrip toolbox [31], which has the magnetic dipole mode implemented, where only the sensor geometry file had to be defined manually.

A measure of the fit quality is the residual variance (RV) between data and model, giving RV = 1.54% for C1 and RV = 2.1% for C2. These small values are corroborated by the high correlation coefficient (ρ) between measured and fitted map, with ρ = 0.988 for C1 and ρ = 0.992 for C2. A significance test is not meaningful with only two correlation coefficients. Instead, the fitted dipole was moved by 5 mm in a random direction resulting in an increased RV to above 25% and ρ dropping below 0.9. The magnetic dipole is a non-linear function of the location and the changes in RV and ρ indicate a location error in the range of a few millimetres.

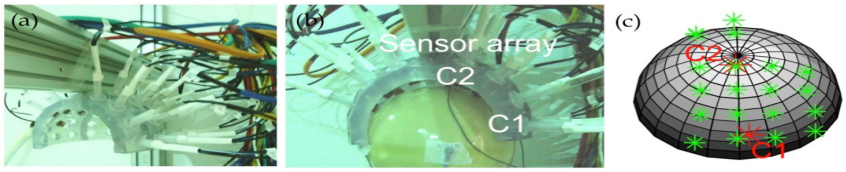

Fig. 5. (a) Photograph of the sensor array suspended on a rigid holder inside a magnetically shielded room. Optical fibers and electrical wires of each sensor are bundle and passed through the magnetically shielded room where they connect to the lasers and electronics. (b) Photograph of the fiberglass sphere holding five small probe coils. Only two of the five probe coils, C1 and C2, were used in the analysis. (c) Sketch showing the relative geometry of the sensors in relation to the two probe coils. Sensors are shown as green stars and the red stars indicate the probe coil positions obtained from the fit with the magnetic dipole model described below.

Optics EXPRESS

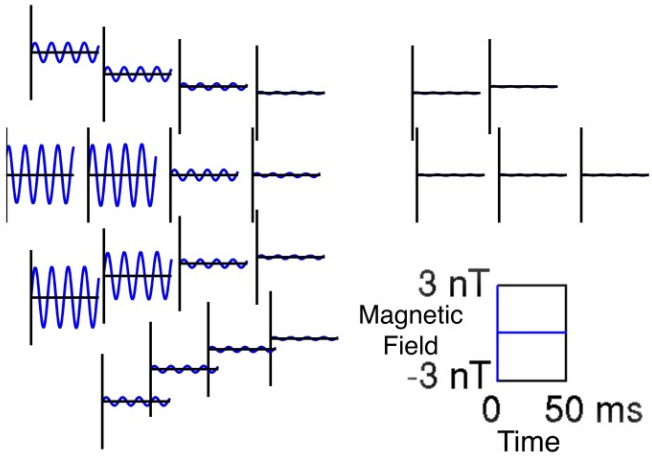

Fig. 6. Averaged signal of coil C1 recorded by the array as a function of time. The figures on the left correspond to the side with the higher channel density, which is the right side in the frontal view photographs in Figs. 5a and 5b. Maximum amplitude of the signals is ~2.5 nT and coil C1 is located close to four channels on the left side of the array. This agrees with the placement shown in Fig. 5b.

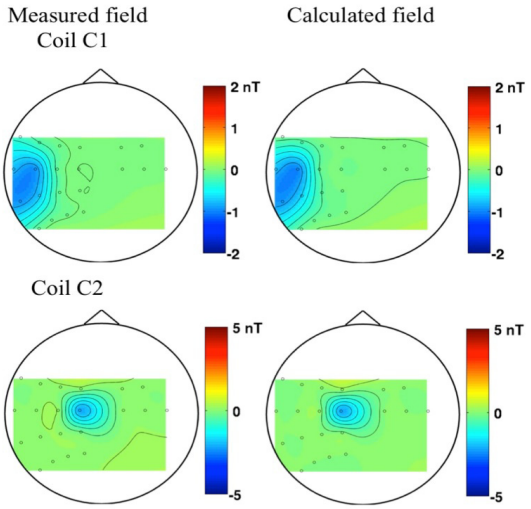

Fig. 7. Magnetic field maps of the two probe coils measured with 21 of our 25-channel imaging array (left) and calculated field map obtained from a fit with the magnetic dipole model (right). The color bar indicates field strength.

5. Summary

We have developed a versatile magnetic imaging system with 25 microfabricated optically-pumped magnetometers. As a proof-of-principle, we have imaged two small coils of diameter 1 cm with the sensor array operating in zero-field mode. Approximating the measured field map with the magnetic dipole model yields convincing results using the least-squares criterion and the correlation between measured and calculated field map. These results demonstrate that the array shows good homogeneity in terms of overall field sensitivity and that the geometric precision of the sensor placement is sufficient to apply simple models, such as the magnetic dipole, to characterize magnetic properties of sources.

Optics EXPRESS

Arrays of OPMs have been used for multichannel recordings such as magnetocardiography [32]. While the potential of OPMs for magnetoencephalography has been demonstrated before [33], the small size and fiber-coupled nature of μOPMs will allow more flexibility in sensor placement and density. This makes them ideally suited for imaging of all kinds of magnetic field sources, including other biomedical applications and non-medical applications such as buried anomaly detection.

Funding

National Institute of Standards and Technology (NIST).

Acknowledgments

We thank Susan Schima for her help with fabrication and assembly.